Journal of Geophysical Research: Atmospheres

RESEARCH ARTICLE
10.1029/2018JD028578

Microphysical and Kinematic Structure of Convective-Scale Elements in the Inner Rainband of Typhoon Matmo (2014) After Landfall

Mingjun Wang[1], Kun Zhao[1], Wen-Chau Lee[2], and Fuqing Zhang[3]

[1]Key Laboratory of Mesoscale Severe Weather/MOE and School of Atmospheric Sciences, Nanjing University, Nanjing, China, [2]National Center for Atmospheric Research, Boulder, CO, USA, [3]Department of Meteorology and Atmospheric Science, The Pennsylvania State University, University Park, PA, USA

Key Points:
- The kinematic structure of convective cells within the inland inner rainband was similar to that of the principal rainband over the ocean
- The hydrometeors within convective regions above the freezing level presented a layered pattern
- Two mechanisms of heavy rainfall formation were identified, predominant warm-rain processes and melting of graupel particles

Correspondence to:
M. Wang,
mjwang@nju.edu.cn

Citation:
Wang, M., Zhao, K., Lee, W.-C., & Zhang, F. (2018). Microphysical and kinematic structure of convective-scale elements in the inner Rainband of Typhoon Matmo (2014) after landfall. *Journal of Geophysical Research: Atmospheres*, *123*. https://doi.org/10.1029/2018JD028578

Received 26 FEB 2018
Accepted 20 MAY 2018
Accepted article online 30 MAY 2018

Abstract The detailed microphysical structure and processes associated with the kinematic structure of the inner rainband of Typhoon Matmo (2014) over East China were examined using observations from an S band polarimetric Doppler radar and an S band Doppler radar. The kinematic structure of convective cells within the inland inner rainband was similar to that of the principal rainband over the ocean in terms of both updrafts and downdrafts. The hydrometeors within convective regions above the freezing level presented a layered pattern, with ice crystals at the top, dry snow in the middle, and graupel at the bottom just above the freezing level. Dry snow and graupel particles were mainly distributed downwind in relation to the overturning updraft. Heavy rainfall occurred mostly in the updraft region and the region affected by graupel. To further investigate the formation of heavy rainfall, variations in reflectivity, differential reflectivity, and rainwater content within different layers were examined. Two distinct mechanisms were identified: (1) in the updraft region the heavy rainfall was predominantly produced through warm-rain processes of autoconversion, accretion, and coalescence between 0.5 and 5 km in altitude; and (2) outside the updraft region, the heavy rainfall was mainly produced through melting of graupel particles. Evaporation was also observed within the radial inflow layer, most likely due to the cool dry air transported by the low-level downdraft. This study revealed, for the first time, the interactions between the microphysical and kinematic structure and the vertical evolution of warm-rain processes in the inner rainbands of tropical cyclones after landfall.

1. Introduction

A tropical cyclone (TC) has long been recognized as an eyewall/rainband complex (Houze, 2010; Willoughby et al., 1984). Within a TC's inner core (the region within ~200 km of the TC center), convection is organized into spiral rainbands (also known as inner rainbands), often accompanied by heavy rainfall and strong wind (e.g., Didlake & Houze, 2009; Samsury & Zipser, 1995). The inner rainbands can play an important role in determining the intensity of TCs by affecting the dynamics at the vortex scale and/or the boundary layer air that transports low-level moist air into the eyewall (G. M. Barnes et al., 1983; Powell, 1990b). Thus, it is vital to better understand the kinematic and microphysical properties of the inner rainbands.

The principal rainband is the most prominent of the inner rainbands. It spirals inward toward the TC center as a quasi-stationary band, with new cells generated at the upwind tail of the rainband (Didlake & Houze, 2009; Houze, 2010; Willoughby et al., 1984). A conceptual model of the kinematic and thermodynamic structure of the principal rainband has been established through extensive observational studies (e.g., G. M. Barnes et al., 1983; Didlake & Houze, 2009, 2013; Hence & Houze, 2008; Powell, 1990a; Tang et al., 2014). The convective-scale circulation of the principal rainband has been summarized as an overturning updraft originating in the inflow layer and two downdrafts, the inner-edge downdraft (IED) and low-level downdraft (LLD), separated by the updraft (Didlake & Houze, 2009; Hence & Houze, 2008; Houze, 2010). The overturning updraft acts to strengthen the midlevel tangential wind jet along the rainband axis through a convergence of the vertical flux of vorticity (Hence & Houze, 2008). The IED, driven by buoyancy pressure gradient acceleration, originates at 6- to 8-km height at the inner boundary of the rainband (Didlake & Houze, 2009). The LLD is forced by the precipitation drag at 2–4 km in the heavy rainfall area, which transports low-θ_e air from the mid-level into the boundary layer inflow (G. M. Barnes et al., 1983; Hence & Houze, 2008). The kinematic structure

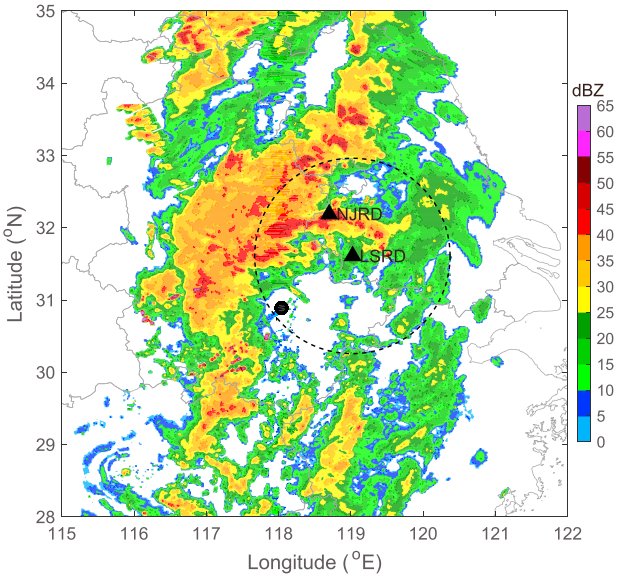

Figure 1. Composite reflectivity (dBZ, color shading) at 1000 UTC July 2014. Solid triangles indicate the locations of the Nanjing radar (NJRD) and Lishui radar (LSRD). The black dot is the location of the typhoon center. The dashed circle indicates the observation range (150 km) of LSRD.

of the inner rainbands has been established mainly using observations over the ocean, whereas, to the best of our knowledge, the TC structure after landfall has not been documented in the literature.

Few studies have examined the microphysical characteristics of the inner rainbands. Aircraft instruments and airborne radars have been used to characterize the microphysical and hydrometeor features of the TC inner core (Black & Hallett, 1986, 1999; Houze et al., 1992; Marks & Houze, 1987), but only indirect information about the inner rainbands has been reported. Aircraft observations have limited temporal and areal coverage because they are restricted to the aircraft's flight path. The Tropical Rainfall Measurement Mission (TRMM) precipitation radar measurements have been used to investigate the vertical structure of TC inner rainbands (Hence & Houze, 2012), although only a rough two-layered structure separated by the freezing level has been revealed.

Polarimetric radars, which have the ability to infer three-dimensional microphysical features at high temporal and spatial resolutions and over long periods, have recently been used to investigate the microphysical characteristics of landfalling TCs (Chang et al., 2009; May et al., 2008; Wang et al., 2016). The graupel and rain/hail mixtures in the eyewall of TC Ingrid were identified for the first time using polarimetric radar analyses (May et al., 2008). Chang et al. (2009) used polarimetric radar measurements to retrieve the drop size distribution (DSD) in the eyewall region of Typhoon Saomai (2006).

Wang et al. (2016; hereafter W16) presented the precipitation microphysics characteristics of the inner rainband (which is not explicitly defined in W16) of Typhoon Matmo (2014) using observations collected by an S band polarimetric radar. Results of their analysis showed that the convective precipitation contains a high number concentration of small- and medium-sized raindrops, and accretion and/or coalescence processes dominate the growth of rainwater below the freezing level. Didlake and Kumjian (2017) investigated the microphysical structure of Hurricane Arthur, using dual-polarization radar observations to examine features of the eyewall, inner rainbands, and outer rainbands in four quadrants relative to the environmental wind shear. Two layers of growth of nonspherical ice particles were identified, with columnar crystals just above the melting level and planar crystals near 8 km in altitude, while the collision-coalescence process was dominant below the melting level due to deep warm clouds in the hurricane.

W16 and Didlake and Kumjian (2017) mainly focused on the overall profiles of dual-polarization signatures of inner rainbands while the convective-scale features of the microphysical structure in the inner rainbands remain to be better documented. The microphysical structures and processes related to the kinematic structures of convective cells, in terms of the updrafts and downdrafts, were examined in this study. As a follow-up of W16, the rainbands of Typhoon Matmo (2014), which were monitored during intensive observation period No. 10 of the Observation, Prediction and Analysis of Severe Convection of China (OPACC) project in 2014, were further examined in the present study. During this period, the eyewall had already broken, with its minimum sea level pressure of ~992 hPa. It was difficult to distinguish the inner rainband from the eyewall/rainband complex after Typhoon Matmo moved inland, although the inner rainband still exhibited features of the principal rainband, such as a spiraling motion inward toward the TC center (Figure 1). New cells were generated in the upwind tail of the rainband and merged with the rainband during its evolution (Figure 2), indicating the distinctive characteristics of the principal rainband. This rainband was located in the region between 120 and 180 km from the TC center and was therefore categorized as the inner rainband in this study (Didlake & Houze, 2013). The rainband was well captured by an S band polarimetric Doppler radar located in Lishui (Lishui Radar: LSRD) and a Chinese Meteorology Administration (CMA) operational S band Doppler radar (Nanjing Radar: NJRD; Figure 1). These radar observations were used in this study to further investigate the microphysical structures and processes of convective cells associated with the kinematic structure of the inner rainband after Matmo's landfall.

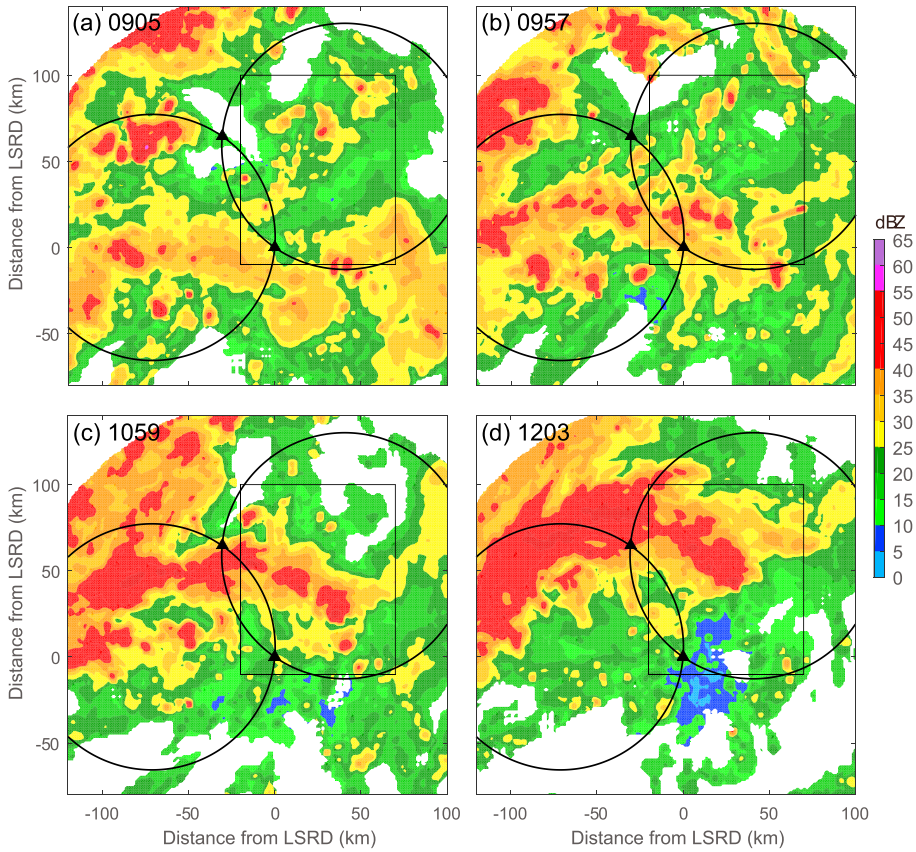

Figure 2. Composite reflectivity (dBZ, color shading) at (a) 0905 UTC, (b) 0957 UTC, (c) 1059 UTC, and (d) 1203 UTC. Triangles are locations of the Nanjing radar (NJRD) and Lishui radar (LSRD). The two circles indicate the optimal region of dual-Doppler analysis. The rectangle indicates the analysis domain.

The paper is organized as follows. Section 2 describes the observations and analysis methods used in this study. The evolution of the convective structure during the cell life cycle is presented in section 3, and the composite kinematic and microphysical structures of the convective cells are shown in section 4. Section 5 examines the formation mechanisms of the heavy rainfall. Section 6 presents conclusions about the microphysical structure of convective cells in the inner rainband and suggests future research directions.

2. Data and Methods

2.1. Radar Data Sets

The same radar data sets as those used in W16 were used in this study. The polarimetric radar data set from LSRD has a 0.92° beam width and a 150-m range resolution and consists of 14 elevations between 0.5° and 19.5°. The NJRD Doppler radar, which is located ~72 km northwest from LSRD, also consists of 14 elevations between 0.5° and 19.5° (Figure 1). The radar reflectivity factors used in this study included horizontal polarization (Z_H), differential reflectivity (Z_{DR}), specific differential phase (K_{DP}), copolar correlation coefficient (ρ_{hv}), and radial velocity (V_r).

The V_r data from LSRD and NJRD were manually edited to unfold the radial velocity, and Z_H data from LSRD and NJRD were also manually edited to remove nonmeteorological echoes. Z_{DR} data measured by LSRD have been well calibrated using several vertical pointing scans at 90° elevation within a light rain region (Bringi & Chandrasekar, 2001), with the differences between LSRD-measured Z_{DR} and two-dimensional video disdrometer (2DVD)-calculated Z_{DR} being $<$0.2 dB (W16). The nonmeteorological measurements of LSRD were removed at $\rho_{hv} < 0.85$. Filters were also applied to Z_H, Z_{DR}, K_{DP}, and ρ_{hv} to reduce the random fluctuations (Schuur et al., 2003; W16).

Table 1
Parameters of the Membership Functions for Eight Classes of Radar Echo

DS	WS	CR	GR	LR	MR	HR	RH
				P [Z_H (dBZ)]			
5	25	0	25	5	30	40	45
10	30	5	35	10	35	45	50
35	40	20	50	35	45	55	75
40	50	25	55	40	50	60	80
				P [Z_{DR} (dB)]			
−0.3	0.5	0.1	−0.3	f_1−0.3	f_1−0.3	f_1−0.3	−0.3
0	1	0.4	0	f_1	f_1	f_1	0
0.3	2	3	f_1	f_2	f_2	f_2	f_1
0.6	3	3.3	f_1 + 0.3	f_2 + 0.5	f_2 + 0.5	f_2 + 0.5	f_1 + 0.5
				P [ρ_{hv}]			
0.95	0.88	0.95	0.90	0.95	0.95	0.92	0.85
0.98	0.92	0.98	0.97	0.97	0.97	0.95	0.9
1.0	0.95	1	1	1	1	1	1
1.01	0.985	1.01	1.01	1.01	1.01	1.01	1.01
				P [LK_{DP}]			
−30	−30	−5	−30	g_1−1	g_1−1	g_1−1	−10
−25	−25	0	−25	g_1	g_1	g_1	−4
10	10	10	10	g_2	g_2	g_2	g_1
20	20	15	20	g_2 + 1	g_2 + 1	g_2 + 1	g_1 + 1

Note. Reflectivity-dependent parameters f_1–f_3 and g_1–g_2 are defined in Park et al. (2009; their equations (4) and (5)). DS = dry snow; WS = wet snow; CR = ice crystal; GR = graupel; LR = light rain; MR = moderate rain; HR = heavy rain; RH = a mixture of rain and hail.

After quality control, the radar data were mapped onto a 1-km horizontal × 0.5-km vertical grid mesh using the U.S. National Center for Atmospheric Research reorder software package (available online at http://www.eol.ucar.edu/rsf/UserGuides/ELDORA/DataAnalysis/reorder/unixreorder.ps). The lowest grid altitude was 0.5 km above ground level. The dual-Doppler wind fields were then synthesized using Cartesian Editing and Display of Radar Data under Interactive Control (CEDRIC) software (Mohr et al., 1986) every 8 min from 1000 UTC to 1200 UTC. The vertical velocity was retrieved through a variational integration scheme within CEDRIC, with a fraction parameter of 0.5 for both the upper and lower boundaries. An 80 × 100-km region extending to an altitude of 15 km was used in this study to cover both the convective rainband and the continuing generation of new updraft cores during 1000 UTC to 1200 UTC (Figure 2).

2.2. Hydrometeor Classification Algorithm

To examine the distribution of hydrometeors within the inner rainband, polarimetric radar data were used by a hydrometeor classification algorithm (HCA) to determine the dominant hydrometeor category at each grid point. The HCA, proposed by Park et al. (2009), was adopted and modified to work on a Cartesian grid used in this study. The texture parameters (standard deviation) of the Z_H field and the differential phase field were only used to identify the nonmeteorological measurements, which had already been removed through the quality control procedure. Thus, only four radar variables were used directly for classification: Z_H, Z_{DR}, ρ_{hv}, and K_{DP}. The raindrop category *big drops* in the original method was eliminated because the rainband generally consisted of a high number concentration of small and medium-sized raindrops (W16). Furthermore, the category *light and moderate rain* used in the original method of Park et al. (2009) was separated into two types: light rain and moderate rain. Finally, the modified HCA in this study included eight classes of radar echoes: dry snow (DS), wet snow (WS), ice crystal (CR), graupel (GR), light rain (LR), moderate rain (MR), heavy rain (HR), and a mixture of rain and hail (RH). The parameters of the membership functions with trapezoidal shapes for every class are presented in Table 1. They were generally adopted from Park et al. (2009), except that the parameters for the Z_H of LR and MR followed Vivekanandan et al. (1999). The reflectivity-dependent parameters f_1–f_3 and g_1–g_2 were adopted from equations (4) and (5) in Park et al. (2009).

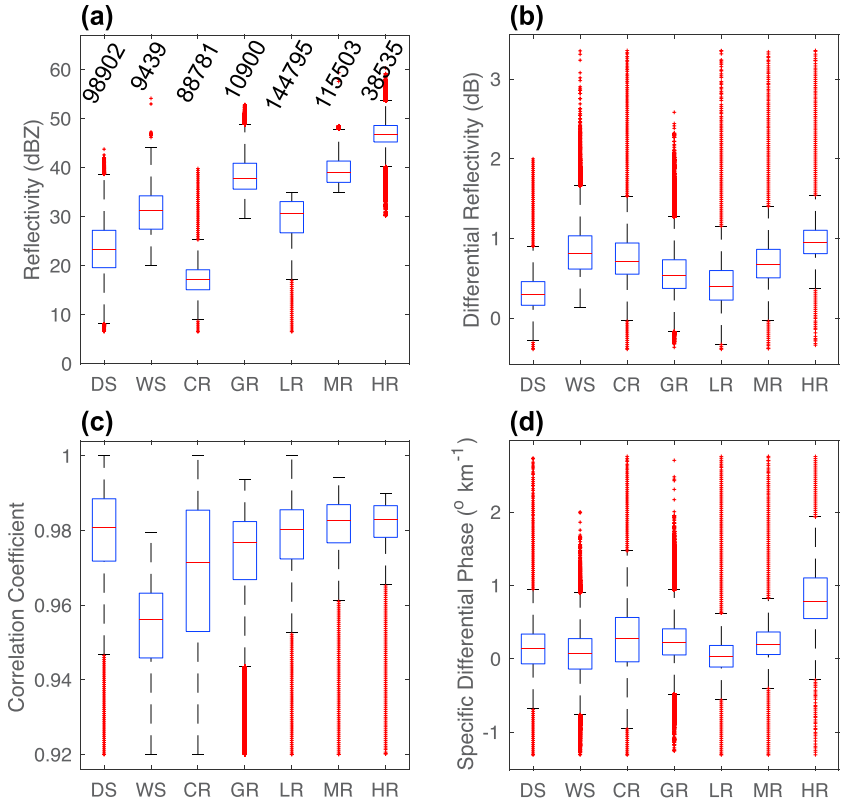

Figure 3. Bar charts showing the distribution of (a) reflectivity, (b) differential reflectivity, (c) the correlation coefficients, and (d) the specific differential phase of all grid points in convective regions with seven hydrometeor species: DS = dry snow; WS = wet snow; CR = ice crystal; GR = graupel; LR = light rain; MR = moderate rain; HR = heavy rain. The red lines are the median, the blue lines are the 25% and 75% quartiles, the black lines represent 99.3% of the data, and the red stars are outliers. The sample count of each category is labeled in (a).

Although the HCA is an extremely powerful tool, it is difficult to validate the retrieved hydrometeor type even with in situ observations because the HCA only identifies the dominant hydrometeor type in a given sample volume. As described in previous studies (Park et al., 2009), each of the eight hydrometeor types was isolated using overlapping membership functions. The HCA can be executed correctly if the hydrometeor types are classified based on unique polarimetric properties. Thus, the analyses of the polarimetric variables for all grid points classified as a given hydrometeor type within the convective regions were calculated to evaluate the performance of the HCA; these are plotted in Figure 3. No RH class was identified; thus, only seven types are shown in Figure 3. The red line in Figure 3 indicates the median of the grid points, the blue box encompasses the data between the 25% and 75% quartiles, the black line represents 99.3% of the data, and the red stars are outliers. Figure 3 shows that the hydrometeor types identified by the HCA were statistically associated with unique polarimetric features in terms of the combinations of Z_H, Z_{DR}, ρ_{hv}, and K_{DP}, suggesting that the HCA was performed correctly. The HCA results are discussed further in sections 3 and 4.

2.3. Microphysical Process Signatures

The hydrometeor categories can represent different ice microphysical processes under the assumption that the hydrometeors are generated locally (Barnes & Houze, 2016). Ice crystal indicates primarily deposition, dry snow represents aggregation along with deposition, graupel indicates riming, most likely combined with deposition, and wet snow represents the occurrence of melting. The assumption is generally valid for this particular case, at least for the graupel particles, since the authors have analyzed the dual-polarimetric variables from dozens of vertical cross sections with graupel being always restricted to a narrow layer just above the freezing level. The possible advection of ice particles would be mentioned to improve the feasibility of this assumption.

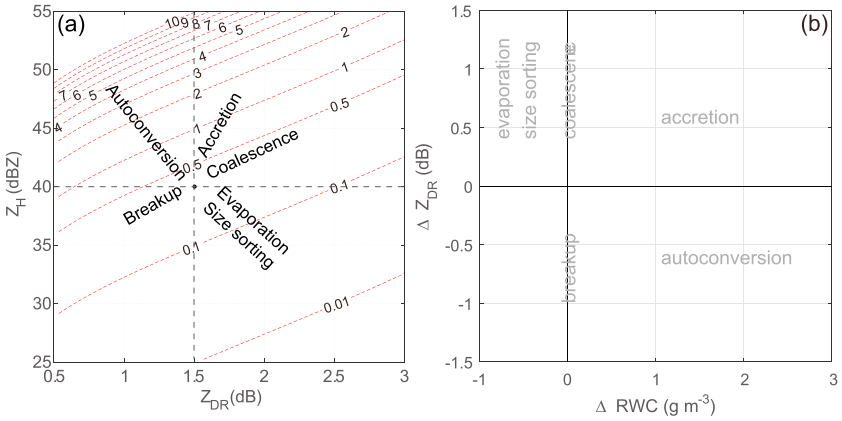

Figure 4. (a) The contours of rainwater content (g/m^3, red dashed lines) according to differential reflectivity − horizontal polarization ($Z_{DR} - Z_H$) within the framework of the constrained-gamma model. (b) Changes in Z_{DR} as a function of changes in rainwater content (RWC). The microphysical processes represented by the variation in Z_{DR}, Z_H, and RWC are annotated.

To identify the dominant warm-rain microphysical processes, Kumjian and Prat (2014) have proposed a parameter space considering the vertical change in Z_H and Z_{DR} over a layer below the freezing level. In the $\Delta Z_H - \Delta Z_{DR}$ coordinates, the coalescence, size sorting/evaporation, breakup, and balance between breakup and coalescence are then represented by the quadrants (Figure 6b of Kumjian & Prat, 2014). However, the accretion process (coalescence of raindrops with cloud droplets) and the autoconversion process (coalescence of cloud droplets to generate drizzle drops) cannot be represented in the diagram, which are generally aliased into the first and fourth quadrants of the parameter space, respectively.

Although the S band polarimetric radar cannot fully capture the status of the cloud (e.g., cloud water content and cloud droplet concentration), the accretion and autoconversion processes can be further identified by including the vertical change in rainwater content (RWC). Both the accretion and autoconversion processes increase the RWC through the conversion of the cloud water into rainwater. By using the constrained-gamma DSD retrieval (Zhang et al., 2001) and the shape-slope ($\mu - \Lambda$) constrain relation derived in W16, the raindrop size distribution $N(D)$ can be retrieved from each pair of Z_H and Z_{DR}. Then, the RWC can be calculated through the formula of $\mathrm{RWC} = \int \frac{\pi}{6}\rho_w D^3 N(D)\mathrm{d}D$, in which ρ_w (1,000 kg/m^3) is the water density. Although the retrieved RWC is not entirely independent of Z_H and Z_{DR}, it provides additional information when the RWC is not available. Figure 4a shows that the RWC distribution is related to Z_H and Z_{DR} within the framework of the constrained-gamma DSD retrieval (Zhang et al., 2001). The increases in Z_H and Z_{DR} along a constant RWC line indicate the coalescence process between raindrops, while the increases in Z_H and Z_{DR} along a trajectory of increasing RWC represent activation of the accretion process. On the other hand, the autoconversion process would produce more small drops with diameters of ~0.1 mm, which will decrease the mean diameter of raindrops, and thus decrease Z_{DR}. The increasing concentration of small raindrops would also increase Z_H and RWC. Thus, the combination of increasing Z_H and decreasing Z_{DR} along a trajectory with increasing RWC indicates the presence of the autoconversion process. The warm-rain processes represented by the variation in Z_{DR} and RWC are summarized in Figure 4b.

2.4. Convective Cell Identification and Radial Cross-Sectional Analysis

To investigate the structure of convective cells, the convective region was identified by reflectivity at an altitude of 2 km using a robust separation algorithm (Steiner et al., 1995; W16). Then, mature convective cells were further identified in terms of updrafts. Following the procedures of Yuter and Houze (1995), the updraft cores with local maximum vertical velocity over 3 m/s were identified. A series of radial (in the radial direction relative to the TC center) vertical cross sections (VCSs) were conducted to examine the vertical structure of mature convective cells. Such VCSs are widely used in studies of inner rainbands (e.g., Didlake & Houze, 2009; Hence & Houze, 2008; Tang et al., 2014). The VCS through the updraft core and

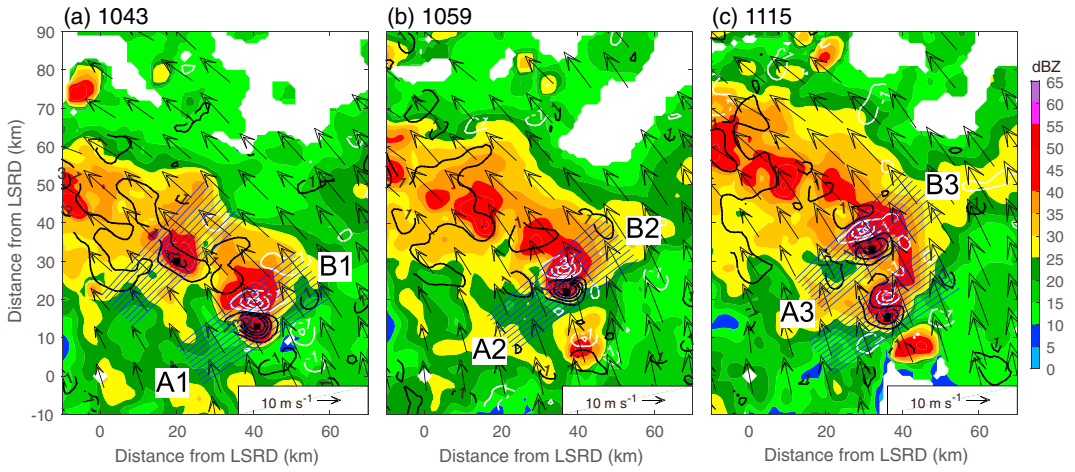

Figure 5. Rainband relative wind vectors, radar reflectivity (dBZ, color shading), and vertical velocities (contours with interval of 2 m/s) at 3 km mean sea level derived from the dual-Doppler synthesis at (a) 1043, (b) 1059, and (c) 1115 UTC. Black (white) contours show updrafts (downdrafts). Line segments indicate the locations of vertical cross sections. The line segments A1–B1, A2–B2, and A3–B3 in each panel mark the vertical cross sections through the maximum vertical velocity of the same cell, which are shown in Figure 6.

TC center was labeled as 0°. Then, VCSs were made through the TC center within an azimuthal range of [−3°, 1.5°] at azimuthal intervals of 0.5° to cover the whole convective cell. Negative (positive) azimuth refers to the downwind (upwind) direction relative to the 0° VCS. The radial axes were centered on the updraft cores with a radial range of [−20 km, 20 km] at radial resolution of 1 km. The TC centers were linearly interpolated from the China Meteorological Administration (CMA) best-track data. Finally, a total of 19 mature convective cells was identified and a total of 190 VCSs was generated and analyzed in the radius-height coordinate system. Figure 5 shows examples of the VCSs. It is clear that each of the convective cells was well covered by the VCSs.

3. Evolution of Convective Cell Structures

The evolution of the kinematic and microphysical structures of one convective cell was tracked and examined. Figure 5 shows the horizontal winds and vertical velocities at 3 km when one of the convective cells was well depicted by the dual-Doppler analysis. Three synthesis periods, 1043, 1059, and 1115 UTC, were chosen to represent the developing (Figure 5a), mature (Figure 5b), and decaying (Figure 5c) stages of the cell. Its updraft cores at different stages were cut by line segments of A1-B1, A2-B2, and A3-B3 (Figure 5), respectively. The horizontal winds were generally parallel to the rainband and had a maximum in the middle of the rainband along the convective cells, which corresponded to the secondary horizontal wind maximum (Hence & Houze, 2008). Intense convective cells with reflectivity over 45 dBZ were embedded in the rainband. New cells were generated in the upwind end, advected downwind, and then merged with the rainband. Individual convective cells displayed a dipole pattern, with upwind updrafts and downwind downdrafts on a spatial scale of ~10 km. An intermittent pattern of updrafts and downdrafts appeared if convective cells were organized as a nearly continuous band (Figures 5b and 5c), which has been recognized as the result of the interactions between cell regeneration and vortex circulation (Didlake & Houze, 2009).

To better understand the vertical structure of the convective cells, the evolution of one convective cell was traced and examined using radial VCSs that cut through the TC center and the maximum updraft (Figure 5). The nearest two VCSs with azimuthal angle of −0.5° and 0.5° were also examined and showed similar evolution of the vertical structure (not shown). The VCSs of Z_H, Z_{DR}, and K_{DP} and the hydrometeor classifications of the cell are shown in Figure 6. The wind vectors exhibit airflows, that is, low-level inflow from the outer to the inner side of the rainband and the overturning updraft (Figure 6), consistent with TC convective cell structures found in previous studies (Didlake & Houze, 2009; Green et al., 2011; Hence & Houze, 2008; Lee et al., 2008; Yu & Tsai, 2013).

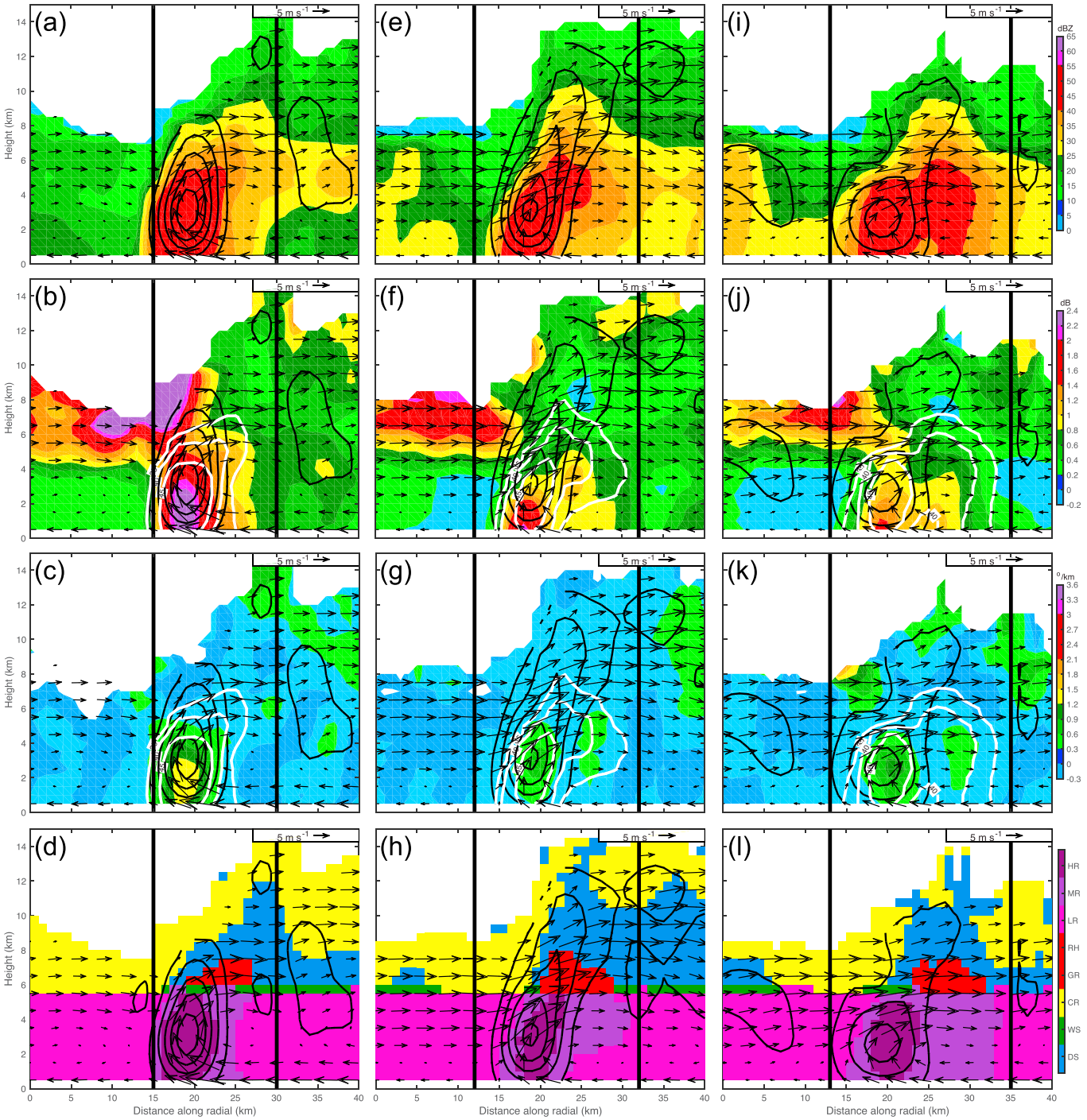

Figure 6. Vertical cross sections of (a) radar reflectivity (dBZ, color shading), (b) differential reflectivity (dB, color shading), (c) specific differential phase (°/km, color shading), and (d) hydrometeor classification (color shading), overlapped by vertical velocities (black contours with an interval of 2 m/s) and band-relative wind vectors along segment A1–B1 in Figure 5. The white lines in (b) and (c) are reflectivity contours of 35, 40, and 45 dBZ. (e)–(h) and (i)–(l) are similar to (a)–(d), except for vertical cross sections along segments A2–B2 and A3–B3 in Figure 5. The thick lines in each panel define the area of convection separated by Steiner et al. (1995).

At 1043 UTC, as the cell was developing, the cores of the updraft, Z_H, Z_{DR}, and K_{DP} were vertically aligned. The strong updrafts were collocated with the strong Z_H, Z_{DR}, and K_{DP}, and hydrometeors of HR (Figures 6a and 6d). The largest Z_{DR} and K_{DP} were present at this stage (Figures 6b and 6c) because heavy rain consisted of median/large raindrops, which can overcome the strong updraft and fall to the ground. Graupel particles

were distributed in the updraft region and the radially downwind side of the updraft. It implies that supercooled liquid water was transported by the strong updraft and the outward radial winds, permitting the occurrence of the riming process and the generation of graupel particles. The graupel particles could also be advected downwind by the outward radial winds. Aggregates (dry snow) showed a similar pattern, with most occurrences in the downwind direction of the updraft. Ice crystals were mainly located at the top of the convective cell.

When the cell became mature (1059 UTC), the updrafts extended to a much higher altitude, over 12 km, than during the developing stage (Figures 6a and 6e). The cell tilted outward in terms of the updraft and reflectivity (Figure 6e). The strong Z_H, Z_{DR}, and K_{DP} and HR hydrometeors were collocated with the strong updrafts (Figures 6e and 6h). The large number of small raindrops generated at this stage resulted in lower Z_{DR} (Figure 6f) compared to the developing stage (Figures 6b and 6c). Consistent with the stronger updrafts, the distribution of graupel extended to a higher altitude and had a wider horizontal spread (Figure 6h), suggesting invigoration of the riming process. A second maximum area of K_{DP} below the freezing level corresponded to the melting graupel outside the updraft (Figures 6g and 6h), implying that graupel particles contributed to the formation of heavy precipitation. Dry snow also had a much deeper and wider distribution (Figure 6h), suggesting that the aggregation process was intensifying.

At 1115 UTC, the cell weakened (Figure 6i). Accordingly, graupels in the updraft were significantly reduced, indicating that the riming process was suppressed due to the limited supercooled liquid water transported by the weakened updraft (Figure 6l). The remaining graupel particles were mostly located downwind of the updraft and were spread by the outward radial wind. The second K_{DP} maximum, the contour of 35 dBZ reflectivity, and moderate rain corresponding to the graupel were further extended toward the ground, further indicating the potential impact of the melting graupel on rainfall intensity. The distribution of dry snow also became shallower and narrower compared to the mature stage (Figure 6l).

In general, the microphysical and kinematic structures were consistent with each other during the evolution of the convective cell. The evolution of microphysical structures, including the polarimetric signature and hydrometeor distribution, was generally driven by the kinematic structure. The aggregation and riming processes become more/less active with a wider/narrower distribution of dry snow and graupel as the updraft intensified/decayed. The distribution of dry snow and graupel was consistent with the strength and spatial extent of the overturning updraft, and the ice crystals were generally at the top of the convective cell. A potential impact of melted graupel on the rainfall was evident during the evolution of the cell. Although only one convective cell was shown, similar evolution was exhibited in other convective cells. A more generalized structure is given in the next section, using the composition of convective cells.

4. Composition of the Convective Cell Structure

To examine the general characteristics of mature convective cells, data from the 190 VCSs were merged to obtain the composite microphysical and kinematic structures of the convective cells in the inner rainband. Averages of Z_H, Z_{DR}, and K_{DP} from all VCSs were calculated and are shown in Figures 7a–7c. The hydrometeor composition was determined by the type with the largest occurrence among all VCSs and is shown in Figure 7d along with the percentage frequency of occurrence of dry snow, graupel, moderate rain, and heavy rain. The vertical velocity and radial wind were also averaged and are overlapped in Figures 7a and 7d. Averages of the updrafts and downdrafts were calculated separately and are overlapped in Figure 7b. The percentage frequency of occurrence of strong updrafts ($\geq$3.0 m/s) and strong downdrafts (≤ -1.5 m/s) in the VCSs were examined and are overlapped in Figure 7c. A lower threshold of strong downdrafts was used because the downdrafts were generally weaker than the updrafts. The composition procedure was performed when valid data samples at a given grid point were over 10% of all VCSs. The threshold only affected the data coverage above 8 km but did not change the structure of both polarimetric and kinematic variables.

The average convective cell in the rainband presented a slightly outward tilting reflectivity tower (Figure 7a), similar to the conceptual model of the principal rainband (Houze, 2010). The overturning updraft originated near the surface and extended to an altitude of 8 km (Figure 7). The low-level radial inflow, extending to an altitude of 2 km from the updraft, penetrated through the updraft and rapidly slowed down (Figure 7a).

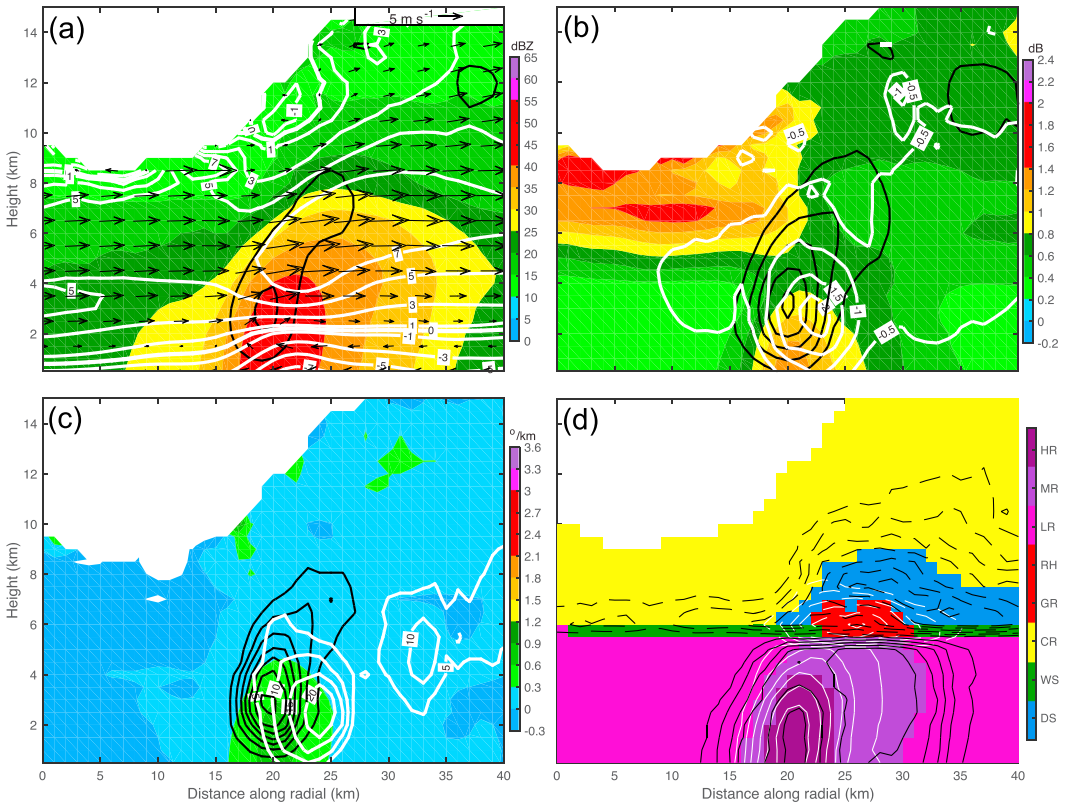

Figure 7. Composite vertical structure of convective cells. (a) Averaged reflectivity (dBZ, color shading), averaged vertical velocity (m/s, black contours), and averaged radial wind speed (m/s, white contours). (b) Averaged differential reflectivity (dB, color shading), averaged updrafts (m/s, black contours), and averaged downdrafts (m/s, white contours). (c) Averaged specific differential phase (°/km, color shading), frequency count in black contours of updrafts ≥3.0 m/s, and frequency count in white contours of downdrafts ≤ − 1.5 m/s. Contours are plotted every 5%, and contours of 5% and greater are shown. (d) The most commonly occurring hydrometeor type among all cross sections (color shading), and frequency counts of heavy rain (HR: solid white contours), moderate rain (MR: solid black contours), graupel (GR: dashed white contours), and dry snow (DS: dashed black contours). Contours of 10% and greater are shown with 10% intervals.

Above the inflow layer was a uniform outflow, with a maximum altitude between 5 and 8 km, which may be due to the superposition of the outflow and the overturning updraft (Figure 7a). The average upward velocity covered a broad area collocated with the reflectivity core, spanning a radial distance of 10 km (Figure 7b), and the average updraft reached a maximum of over 5 m/s at an altitude of 3 km (Figure 7b). In previous studies (Didlake & Houze, 2009, 2013; Hence & Houze, 2008; Yu & Tsai, 2013), the updraft was mainly located at the inner edge of the inner rainband, meaning that heavy rainfall generally occurred radially outside the updraft. However, the updraft was collocated with the heavy rainfall in this case, which may be attributed to the less tilted structure and different processes, that is, a warm-rain-dominant or ice phase-dominant process, producing heavy rainfall.

Figure 7b also reveals two branches of downdrafts separated by the updraft core. One was located radially outward of the updraft core and had a maximum velocity of over 2 m/s near an altitude of 2.5 km, which is the LLD described by Didlake and Houze (2009). Another downdraft center, much weaker than the LLD, was located radially inward of the updraft core between 2 and 6 km. This downdraft appeared to be the IED depicted in Didlake and Houze (2009), although the vertical extension and intensity were different. The most frequent strong updrafts over 35% of the VCSs were located in almost the same location as the maximum updraft (Figure 7c). Only strong LLDs were evident in the frequency distribution because there was no IED of over 1.5 m/s (Figure 6c). In general, the kinematic structure was consistent with the conceptual model of the principal rainband being observed over the ocean summarized in the literature (e.g., Didlake & Houze, 2009; Hence & Houze, 2008).

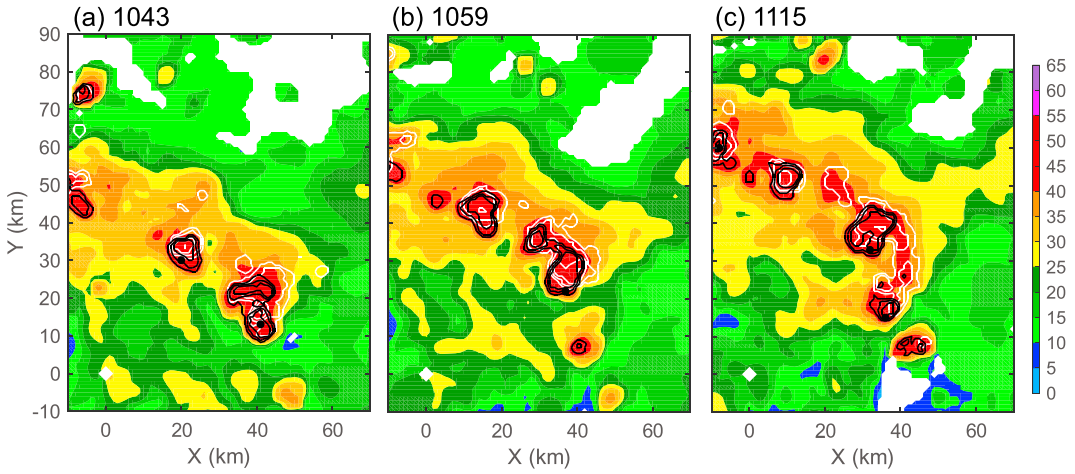

Figure 8. Reflectivity at an altitude of 3 km (dBZ, color shading), number of levels with heavy rain from 2 to 5 km (black contours), and number of levels with graupel above the freezing level (white contours) at (a) 1043, (b) 1059, and (c) 1115 UTC. Contours are shown from 1 with intervals of 1. The black dots in each panel indicate the locations of the updraft centers.

There were Z_{DR} and K_{DP} maxima corresponding to the reflectivity and updraft core, (Figures 7a–7c). It was clear that the Z_{DR} and K_{DP} increased toward the ground (Figures 7b and 7c), which was consistent with the statistics of the polarimetric variables in the convective region in W16. A region with a Z_{DR} over 1 dB above the freezing level at the upwind portion of the rainband was recognized as a location where ice crystals were dominant (Figures 7b and 7d). These were most likely columnar crystals transported from the dissipating eyewall (Black & Hallett, 1999; Houze, 2010).

The hydrometeors above the freezing level presented a layered pattern, as mentioned previously, with ice crystal at the top, dry snow at the middle, and graupel at the bottom just above the freezing level (Figure 7d). Graupel and dry snow mostly originated due to the updraft and/or were spread downwind by the outward radial wind (Figure 7d) and the tangential wind (not shown). Dry snow could extend to altitudes over 10 km, whereas the graupel generally occurred below 8 km. The largest occurrence of graupel was collocated with the strong downdrafts below the freezing level (Figures 7c and 7d), suggesting that the drag effect of the melted graupel was vital for the formation of the LLD. The graupel had almost the same horizontal distribution as the moderate rain, with a 10% frequency of both graupel and moderate rain (Figure 7d). The heavy rain occurred most frequently in the updraft region and with lower frequency in the region covered by the graupel, indicating that the generation of heavy rain can be attributed to the strong updraft and melting of graupel. The impacts of the updraft and graupel were examined; the results are given in the next section.

5. Formation Mechanisms of Heavy Rainfall

To further examine the connection between heavy rain, updrafts, and graupel, the horizontal distribution of heavy rain, updrafts, and graupel at 1043, 1059, and 1115 UTC, shown in Figure 8, was examined. The graupel was generally distributed in the downwind direction (both radial and tangential direction) of the updrafts. Consistent with the composite analyses, the horizontal distributions of heavy rain were generally connected with the updrafts and the graupel aloft. The graupel had broader coverage than heavy rain did (Figure 8), which was consistent with the wider radial extent of graupel (Figure 7). The heavy rain was generally collocated with the updrafts when the cell was developing (Figure 8a). With the evolution of the convective cells, the cells become tilted, and the occurrence of heavy rain increased downwind of the updrafts (Figures 8b and 8c), which was expected and consistent with the vertical structure. The overlapped regions of the heavy rain and graupel were collocated with the convective downdrafts (Figures 5 and 8), which was consistent with cooling and the drag effects of melting graupel. During the period between 1000 and 1200 UTC, ~72% of heavy rain occurred in the updraft region, ~50% of heavy rain occurred in the region affected by graupel, and ~22% of heavy rain were in the region with both updraft and graupel.

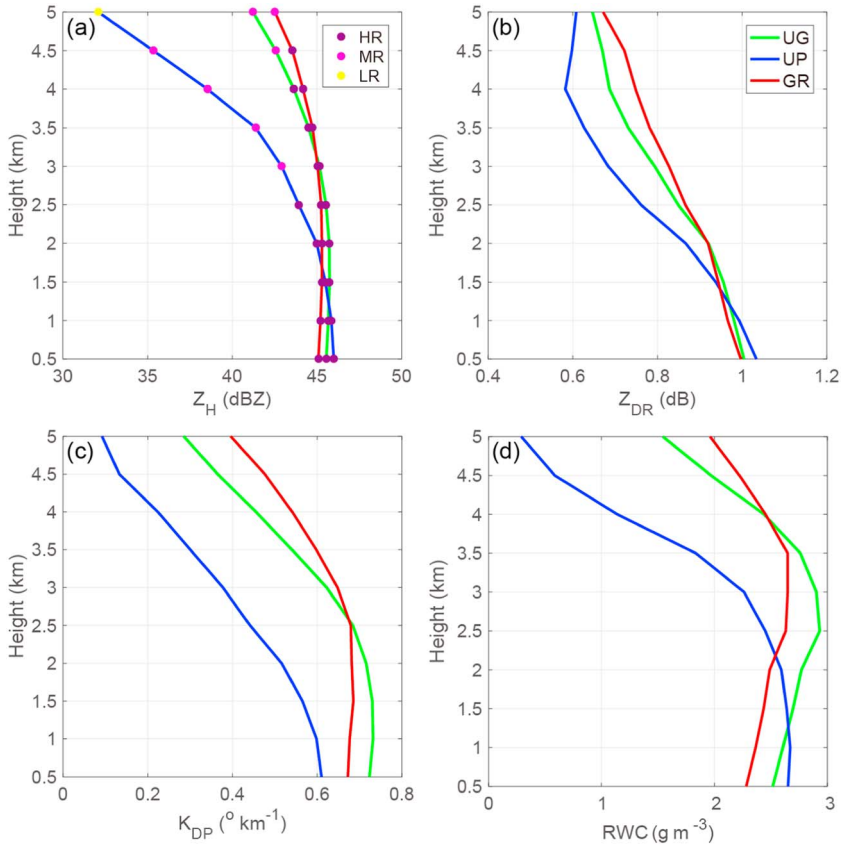

Figure 9. Vertical profiles of the (a) reflectivity, (b) differential reflectivity, (c) specific differential phase, and (d) rainwater content (RWC) within heavy rainfall (HR) regions affected by updraft, graupel, and both. The colored dots represent the dominant hydrometeor at each level.

To examine the impacts of updrafts and graupel particles on the heavy rainfall, three regions with HR were defined: a region only affected by updrafts at a height of 3 km (UP region), a region with graupel aloft (GR region), and a region with both updrafts at a height of 3 km and graupel aloft (UG region). The updrafts were generally vertically aligned below the freezing level and directly affected the warm-rain processes. Thus, the updrafts at a height of 3 km were chosen as representative. Generally, the UP, GR, and UG regions represent the updraft region, the downdraft region, and the region between updrafts and downdrafts, respectively.

Figure 9 shows the vertical profiles of Z_H, Z_{DR}, and K_{DP} and the hydrometeors within the UP, GR, and UG regions below 5 km, well below the ambient freezing level of 5.5 km. In general, there were distinct differences in the polarimetric profiles among the three regions. Within the UP region, Z_H, K_{DP}, and RWC growth increased rapidly toward the ground for the dominant hydrometeor types varying from light rain to heavy rain, and Z_{DR} decreased until 4 km and then increased toward the ground. This suggests the rapid growth of rainwater and the presence of complex warm-rain processes. With the melting of graupel, Z_H, Z_{DR}, K_{DP}, and RWC were much larger at 5 km for the moderate rain in the GR and UG regions. The GR region had the lowest rate of increase for Z_H, Z_{DR}, and K_{DP}, and the Z_H and Z_{DR} were lower than those in the UP region below 1.5 km. The variations in polarimetric variables within the UG region were closer to those of the GR than of the UP region, suggesting that the melting graupel had a large impact when the updraft was relatively weak.

In W16, the Z_H and Z_{DR} changed from 5 to 2 km within the convective region of the whole rainband, indicating that the growth of RWC was mainly achieved through the warm-rain processes. The RWC paths in this study (Figure 9d) clearly showed two different mechanisms producing heavy rainfall: pure warm-rain production within the UP region and the melting of graupel produced by active ice processes within the GR region. Due to the prevalence of updrafts in the heavy rainfall region, the rainband was characterized

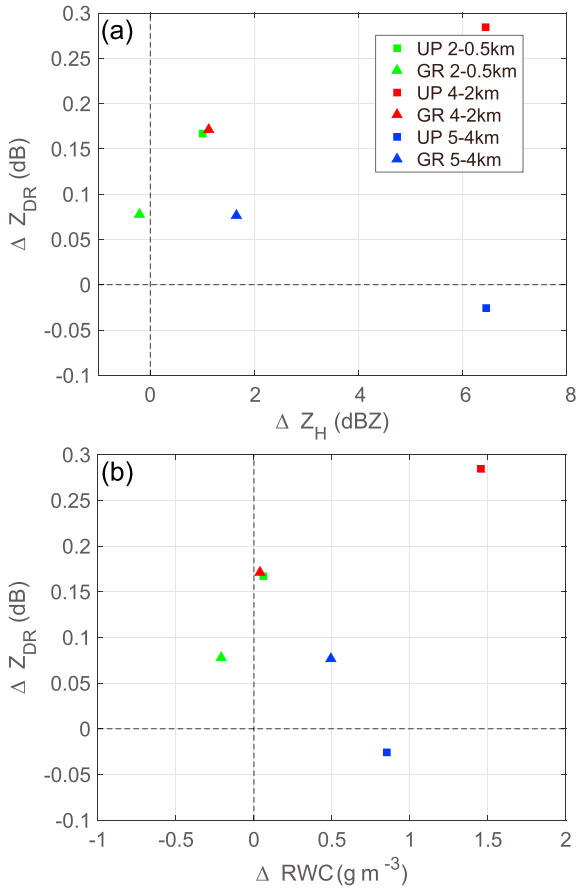

Figure 10. Mean variations in (a) differential reflectivity (Z_{DR}) and horizontal polarization (Z_H), and (b) Z_{DR} and rainwater content (RWC) for the UP (squares) and GR (triangles) regions from 5 to 4 km (blue markers), from 4 to 2 km (red markers), and from 2 to 0.5 km (green markers).

by the dominance of RWC growth through warm-rain processes. The changes in Z_H, Z_{DR}, K_{DP}, and RWC in this study indicated complex variations in warm-rain processes in the different vertical layers and different horizontal regions, which require further investigation.

Before examining the warm-rain processes, the cloud water distribution was estimated according to the kinematic structure. The rainband had a moist environment, with relative humidity over 95% near the surface and overall relative humidity over 80% below the freezing level (W16), indicating a sufficient water vapor supply. Cloud droplets form in the atmosphere when ascending air reaches equilibrium saturation. If ascent continues, supersaturation is produced by the cooling, and the cloud droplets grow by diffusion of water vapor. The number concentration of cloud droplets and the supersaturation are generally proportional to the vertical velocity (Hudson & Noble, 2014; Lu et al., 2012), suggesting that the updraft region would have higher cloud water content than would the other regions. After the cloud formed, its distribution would be further influenced by advection. Therefore, the downwind regions related to the updrafts were expected to have a net cloud water advection above the radial inflow layer with a radius of 20–30 km due to the radial outflow (Figure 7). Generally, the advection of the cloud water would decrease with height according to the outward radial winds. In comparison, the radial inflow layer below 2 km would have much lower cloud water content in terms of the generation and advection of cloud droplets.

Because the UG region was similar to the GR region, the microphysical processes of the UP and GR regions were examined. Figure 10 shows the mean variations in $Z_H - Z_{DR}$ and RWC $- Z_{DR}$ calculated from all grid points within the UP and GR regions for three different layers, 4–5, 2–4, and 0.5–2 km. Within the UP area, the averaged Z_H increased over 6 dBZ (Figures 9a and 10a), and the averaged RWC increased ~0.8 g/m^3 (Figure 10b), while the averaged Z_{DR} slightly decreased (Figure 10). A plausible explanation for such a unique signature is that the autoconversion process was activated due to the high concentration of cloud droplets within this layer of the UP region. Within the GR region, the averaged Z_H, Z_{DR}, and RWC increased slightly by ~2 dBZ, ~0.08 dB, and ~0.5 g/m^3, respectively, suggesting that the accretion process was dominant in the GR region from 5 to 4 km.

From 4 down to 2 km, the Z_H, Z_{DR}, and RWC continued to increase within the UP region, with the mean Z_H increasing from 39 to 45 dBZ, the averaged Z_{DR} increasing from 0.55 to 0.83 dB, and RWC growth of ~1.5 g/m^3 (Figures 9 and 10). These signatures clearly represent the dominance of the accretion process, possibly along with the autoconversion and coalescence processes, consistent with the high cloud water content in the UP region. In the GR region, the averaged Z_H and Z_{DR} increased by ~1.2 dBZ and ~0.17 dB (Figure 10a), respectively, while the RCW did not change (Figure 10b). Due to the reduced cloud water content within this layer in the GR region, the $Z_H - Z_{DR}$ and RWC $- Z_{DR}$ signatures clearly indicated a coalescence between raindrops, which increased the Z_H and Z_{DR}, with a constant RWC.

Within the inflow layer descending from 2 to 0.5 km, Z_H and Z_{DR} continued to grow with the same RWC (Figures 9 and 10), indicating the dominance of the coalescence process in the UP region. In the GR region there was an increase in the averaged Z_{DR}, a slight decrease in the averaged Z_H (Figure 10a), and a decrease in the RWC of about 0.2 g/m^3 (Figure 10b). This most likely indicated the occurrence of an evaporation process, which could be attributed to the cool and dry air brought into the inflow layer by the LLD.

In general, all the requirements for warm-rain generation were present in the UP region: the initiation of raindrops through autoconversion and the growth of raindrops through accretion and coalescence processes. The RWC grew rapidly with the higher cloud water content in the updraft area through the

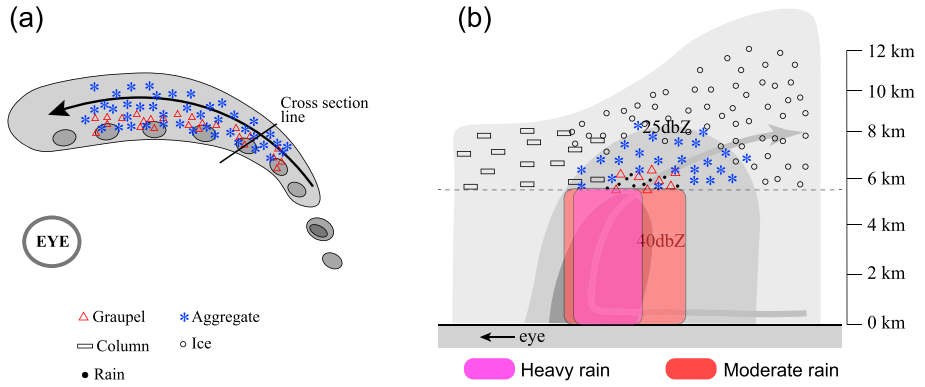

Figure 11. Schematic showing the location of different types of hydrometeor relative to the kinematic structure in (a) horizontal and (b) vertical directions. The gray arrow in (b) indicates the overturning updraft. The gray dashed line represents the freezing level.

autoconversion and accretion processes. In comparison, graupel contributed to the heavy rainfall mainly by melting into rainwater below the freezing level within GR region. There was no direct observation of cloud structure, and therefore, studies with cloud observations and/or an in situ verification should be conducted in the future.

6. Conclusions and Discussions

In this study, the convective structures of the inner rainband of Typhoon Matmo (2014) were investigated using the microphysical information from an S band polarimetric Doppler radar and the kinematic fields derived from the dual-Doppler synthesis. The evolution of the microphysical structure of convective cells associated with the kinematic structure was examined, including the polarimetric structure and the dominant hydrometeor distribution. The formation mechanisms of heavy rainfall related to the kinematic and microphysical structures were further investigated by analyzing the growth of the RWC below the freezing level to the ground.

The composite of all convective cells in the rainband presented the general characteristics of microphysical and kinematic structures. The composite kinematic structure was generally consistent with the conceptual model of the principal rainband summarized in the literature in terms of the overturning updraft, the inner edge downdraft, and the LLD. The hydrometeors above the freezing level presented a layered pattern, with ice crystals at the top, dry snow in the middle, and graupel at the bottom just above the freezing level. Graupel particles were generally produced in the region with the supercooled liquid water transported by the updraft and were also advected downwind by the airflow. The largest occurrence of graupel was collocated with the strong downdrafts below the freezing level, meaning that the drag effect of the melted graupel can be attributed to the formation of the LLD. Heavy rain occurred most frequently in the updraft region and was generated with lower frequency in the graupel region, while moderate rain occurred in the region with graupel aloft. A schematic model of hydrometeor distribution associated with the overturning updraft is given in Figure 11.

Unlike the conceptual structure revealed in previous studies for oceanic TC inner rainbands, the heavy rain of the inner rainband in this study mostly occurred in the updraft region, rather than outside the updraft. The vertical profiles of Z_H, Z_{DR}, and RWC from an altitude of 5 to 0.5 km indicated two distinct mechanisms of heavy rainfall formation: the growth of RWC through warm-rain production within the updraft region and the melting of graupel particles outside the updraft region. The precipitation in the updraft region was initiated with raindrops generated through the autoconversion process immediately below the freezing level. The RWC then grew rapidly toward the ground through accretion and/or autoconversion processes, while the coalescence process was dominant within the radial inflow layer below 2 km. In comparison, the heavy rainfall outside the updraft region was mainly produced by the melting of graupel particles and from a secondary source of RWC growth through the accretion process. Evaporation occurred within the radial inflow layer most likely due to the cool dry air transported by the downdrafts.

The distribution of hydrometeor types relative to the convective updraft cores in this study was quite similar to that of tropical mesoscale convective systems (MCSs) during the active stage of the Madden-Julian Oscillation (Barnes & Houze, 2014; their Figure 7 and Figure 8), suggesting that the hydrometeor distribution in the rainband was generally reliable. Also, it may imply that the hydrometeor distribution strongly depends on the kinematic structure. One notable difference was that heavy rain occurs downwind of the updraft core in MCSs. This may be attributed to the different intensities of updrafts, and the different mechanisms of heavy rainfall formation, for example, warm-rain dominant or ice process dominant.

In W16, the fast growth of the RWC was generally attributed to the accretion process based on the variation in Z_H, Z_{DR}, and RWC between 5 and 2 km in altitude. In this study, a more detailed vertical evolution of warm-rain processes was revealed. One interesting finding was that the autoconversion process was observed within the layer between 4 and 5 km and most likely also occurred below 4 km. Such a process produces small raindrops and may explain the extremely high number concentration of small raindrops in this rainband. This would be an interesting topic to investigate in combination with a numerical model. Some of the explanations in this study were based on physical speculations regarding the cloud water distribution; thus, observations of the number concentration and size of the cloud droplets will be important for future studies of the warm-rain processes in the mixed-phase precipitation. Also, it would be interesting to perform an ice particle trajectory analysis based on the high-resolution numerical simulation in the future.

Acknowledgments

This work was primarily supported by the National Natural Science Foundation of China (grant 41605026), Guangzhou Municipal Science and Technology Planning Project (grant 201604020069), and the National Fundamental Research 973 Program of China (2013CB430101). We would also like to acknowledge the China Meteorological Administration and PLA University of Science and Technology for collecting and archiving the radar data used in this study. Data used in this work are from the National Fundamental Research 973 Program of China (2013CB430101). The data used in this study are available on ftp://radar.nju.edu.cn, with the username of jgr and the password of jgr. The English language in this document has been checked by at least two professional Editors, both native speakers of English. For a certificate, please see http://www.textcheck.com/certificate/hwd8ex.

References

Barnes, G. M., Zipser, E. J., Jorgensen, D., & Marks, F. (1983). Mesoscale and convective structure of a hurricane rainband. *Journal of the Atmospheric Sciences*, *40*(9), 2125–2137. https://doi.org/10.1175/1520-0469(1983)040%3C2125:MACSOA%3E2.0.CO;2

Barnes, H. C., & Houze, R. A. (2014). Precipitation hydrometeor type relative to the mesoscale airflow in mature oceanic deep convection of the Madden-Julian Oscillation. *Journal of Geophysical Research: Atmospheres*, *119*, 13,990–14,014. https://doi.org/10.1002/2014JD022241

Barnes, H. C., & Houze, R. A. (2016). Comparison of observed and simulated spatial patterns of ice microphysical processes in tropical oceanic mesoscale convective systems. *Journal of Geophysical Research: Atmospheres*, *121*, 8269–8296. https://doi.org/10.1002/2016JD025074

Black, R. A., & Hallett, J. (1986). Observations of the distribution of ice in hurricanes. *Journal of the Atmospheric Sciences*, *43*(8), 802–822. https://doi.org/10.1175/1520-0469(1986)043%3C0802:OOTDOI%3E2.0.CO;2

Black, R. A., & Hallett, J. (1999). Electrification of the hurricane. *Journal of the Atmospheric Sciences*, *56*(12), 2004–2028. https://doi.org/10.1175/1520-0469(1999)056%3C2004:EOTH%3E2.0.CO;2

Bringi, V. N., & Chandrasekar, V. (2001). *Polarimetric Doppler Weather Radar: Principles and Applications*. Cambridge, UK: Cambridge University Press. https://doi.org/10.1017/CBO9780511541094

Chang, W.-Y., Wang, T.-C. C., & Lin, P.-L. (2009). Characteristics of the raindrop size distribution and drop shape relation in typhoon systems in the western Pacific from the 2D video disdrometer and NCU C-band polarimetric radar. *Journal of Atmospheric and Oceanic Technology*, *26*(10), 1973–1993. https://doi.org/10.1175/2009JTECHA1236.1

Didlake, A. C., & Houze, R. A. (2009). Convective-scale downdrafts in the principal rainband of Hurricane Katrina (2005). *Monthly Weather Review*, *137*(10), 3269–3293. https://doi.org/10.1175/2009MWR2827.1

Didlake, A. C., & Houze, R. A. (2013). Convective-scale variations in the inner-core rainbands of a tropical cyclone. *Journal of the Atmospheric Sciences*, *70*(2), 504–523. https://doi.org/10.1175/JAS-D-12-0134.1

Didlake, A. C., & Kumjian, M. R. (2017). Examining polarimetric radar observations of bulk microphysical structures and their relation to vortex kinematics in Hurricane Arthur (2014). *Monthly Weather Review*, *145*(11), 4521–4541. https://doi.org/10.1175/MWR-D-17-0035.1

Green, B. W., Zhang, F., & Markowski, P. M. (2011). Multiscale processes leading to supercells in the landfalling outer rainbands of Hurricane Katrina (2005). *Weather and Forecasting*, *26*(6), 828–847. https://doi.org/10.1175/WAF-D-10-05049.1

Hence, D. A., & Houze, R. A. (2008). Kinematic structure of convective-scale elements in the rainbands of Hurricanes Katrina and Rita (2005). *Journal of Geophysical Research*, *113*, D15108. https://doi.org/10.1029/2007JD009429

Hence, D. A., & Houze, R. A. (2012). Vertical structure of tropical cyclone rainbands as seen by the TRMM precipitation radar. *Journal of the Atmospheric Sciences*, *69*(9), 2644–2661. https://doi.org/10.1175/JAS-D-11-0323.1

Houze, R. A. (2010). Clouds in tropical cyclones. *Monthly Weather Review*, *138*(2), 293–344. https://doi.org/10.1175/2009MWR2989.1

Houze, R. A., Marks, F. D., & Black, R. A. (1992). Dual-aircraft investigation of the inner core of Hurricane Norbert. Part II: Mesoscale distribution of ice particles. *Journal of the Atmospheric Sciences*, *49*(11), 943–963. https://doi.org/10.1175/1520-0469(1992)049%3C0943:DAIOTI%3E2.0.CO;2

Hudson, J. G., & Noble, S. (2014). CCN and vertical velocity influences on droplet concentrations and supersaturations in clean and polluted stratus clouds. *Journal of the Atmospheric Sciences*, *71*(1), 312–331. https://doi.org/10.1175/JAS-D-13-086.1

Kumjian, M. R., & Prat, O. P. (2014). The impact of raindrop collisional processes on the polarimetric radar variables. *Journal of the Atmospheric Sciences*, *71*(8), 3052–3067. https://doi.org/10.1175/JAS-D-13-0357.1

Lee, W.-C., Bell, M. M., & Goodman, K. E. Jr. (2008). Supercells and mesocyclones in the outer rainbands of Hurricane Katrina (2005). *Geophysical Research Letters*, *35*, L16803. https://doi.org/10.1029/2008GL034724

Lu, C., Liu, Y., Niu, S., & Vogelmann, A. M. (2012). Observed impacts of vertical velocity on cloud microphysics and implications for aerosol indirect effects. *Geophysical Research Letters*, *39*, L21808. https://doi.org/10.1029/2012GL053599

Marks, F. D., & Houze, R. A. (1987). Inner core structure of Hurricane Alicia from airborne Doppler radar observations. *Journal of the Atmospheric Sciences*, *44*(9), 1296–1317. https://doi.org/10.1175/1520-0469(1987)044%3C1296:Icsoha%3E2.0.co;2

May, P. T., Kepert, J. D., & Keenan, T. D. (2008). Polarimetric radar observations of the persistently asymmetric structure of Tropical Cyclone Ingrid. *Monthly Weather Review*, *136*(2), 616–630. https://doi.org/10.1175/2007MWR2077.1

Mohr, C. G., Jay Miller, L., Vaughan, R. L., & Frank, H. W. (1986). The merger of mesoscale datasets into a common Cartesian format for efficient and systematic analyses. *Journal of Atmospheric and Oceanic Technology*, *3*(1), 143–161. https://doi.org/10.1175/1520-0426(1986)003%3C0143:TMOMDI%3E2.0.CO;2

Park, H. S., Ryzhkov, A. V., Zrnić, D. S., & Kim, K.-E. (2009). The hydrometeor classification algorithm for the polarimetric WSR-88D: Description and application to an MCS. *Weather and Forecasting*, *24*(3), 730–748. https://doi.org/10.1175/2008WAF2222205.1

Powell, M. D. (1990a). Boundary layer structure and dynamics in outer hurricane rainbands. Part I: Mesoscale rainfall and kinematic structure. *Monthly Weather Review*, *118*(4), 891–917. https://doi.org/10.1175/1520-0493(1990)118%3C0891:BLSADI%3E2.0.CO;2

Powell, M. D. (1990b). Boundary layer structure and dynamics in outer hurricane rainbands. Part II: Downdraft modification and mixed layer recovery. *Monthly Weather Review*, *118*(4), 918–938. https://doi.org/10.1175/1520-0493(1990)118%3C0918:BLSADI%3E2.0.CO;2

Samsury, C. E., & Zipser, E. J. (1995). Secondary wind maxima in hurricanes: Airflow and relationship to rainbands. *Monthly Weather Review*, *123*(12), 3502–3517. https://doi.org/10.1175/1520-0493(1995)123%3C3502:SWMIHA%3E2.0.CO;2

Schuur, T., Ryzhkov, A., Heinselman, P., Zrnic, D., Burgess, D., & Scharfenberg, K. (2003). Observations and classification of echoes with the polarimetric WSR-88D radar (p. 46). NOAA/National Severe Storms Laboratory rep.

Steiner, M., Houze, R. A., & Yuter, S. E. (1995). Climatological characterization of three-dimensional storm structure from operational radar and rain gauge data. *Journal of Applied Meteorology*, *34*(9), 1978–2007. https://doi.org/10.1175/1520-0450(1995)034%3C1978:CCOTDS%3E2.0.CO;2

Tang, X., Lee, W.-C., & Bell, M. (2014). A squall-line-like principal rainband in Typhoon Hagupit (2008) observed by airborne Doppler radar. *Journal of the Atmospheric Sciences*, *71*(7), 2733–2746. https://doi.org/10.1175/JAS-D-13-0307.1

Vivekanandan, J., Ellis, S. M., Oye, R., Zrnić, D. S., Ryzhkov, A. V., & Straka, J. (1999). Cloud microphysics retrieval using S-band dual-polarization radar measurements. *Bulletin of the American Meteorological Society*, *80*(3), 381–388. https://doi.org/10.1175/1520-0477(1999)080%3C0381:CMRUSB%3E2.0.CO;2

Wang, M., Zhao, K., Xue, M., Zhang, G., Liu, S., Wen, L., & Chen, G. (2016). Precipitation microphysics characteristics of a Typhoon Matmo (2014) rainband after landfall over Eastern China based on polarimetric radar observations. *Journal of Geophysical Research: Atmospheres*, *121*, 12,415–12,433. https://doi.org/10.1002/2016JD025307

Willoughby, H. E., Jin, H.-L., Lord, S. J., & Piotrowicz, J. M. (1984). Hurricane structure and evolution as simulated by an axisymmetric, nonhydrostatic numerical model. *Journal of the Atmospheric Sciences*, *41*(7), 1169–1186. https://doi.org/10.1175/1520-0469(1984)041%3C1169:HSAEAS%3E2.0.CO;2

Yu, C.-K., & Tsai, C.-L. (2013). Structural and surface features of arc-shaped radar echoes along an outer tropical cyclone rainband. *Journal of the Atmospheric Sciences*, *70*(1), 56–72. https://doi.org/10.1175/JAS-D-12-090.1

Yuter, S. E., & Houze, R. A. (1995). Three-dimensional kinematic and microphysical evolution of Florida cumulonimbus. Part I: Spatial distribution of updrafts, downdrafts, and precipitation. *Monthly Weather Review*, *123*(7), 1921–1940. https://doi.org/10.1175/1520-0493(1995)123%3C1921:TDKAME%3E2.0.CO;2

Zhang, G., Vivekanandan, J., & Brandes, E. (2001). A method for estimating rain rate and drop size distribution from polarimetric radar measurements. *IEEE Transactions on Geoscience and Remote Sensing*, *39*(4), 830–841. https://doi.org/10.1109/36.917906